A finite element procedure for radio-frequency sheath-plasma interactions in the ion cyclotron range of frequencies

H. Kohno[a,*], J.R. Myra[b], D.A. D'Ippolito[b]

[a] *Plasma Science and Fusion Center, Massachusetts Institute of Technology, 77 Massachusetts Avenue, Cambridge, MA 02139, USA*
[b] *Lodestar Research Corporation, 2400 Central Avenue P-5, Boulder, CO 80301, USA*

Abstract

A numerical code that solves self-consistent radio-frequency (RF) sheath-plasma interactions in the ion cyclotron range of frequencies is developed based on a nonlinear finite element technique. The present code solves for plasma waves based on the cold plasma model subject to a sheath boundary condition. The finite element procedure has been implemented for one- and two-dimensional analyses using simplified models for the poloidal plane of a tokamak. The results show good accuracy and generalize previous analytical calculations. The present approach shows promise for developing a code to predict RF sheath potentials in the scrape-off layer of RF-heated fusion experiments.

Keywords: Plasma waves, Radio-frequency sheaths, Cold plasma, Magnetic confinement fusion, Finite element method, High performance computing

1. Introduction

Nuclear-fusion power generation is considered one of the promising candidates in order to support worldwide massive energy consumption in a safe and environmentally-friendly way [1]. Fusion occurs in high temperature

*Corresponding author
Email addresses: kohno@alum.mit.edu (H. Kohno), jrmyra@lodestar.com (J.R. Myra), dippolito@lodestar.com (D.A. D'Ippolito)

plasmas, and requires a critical combination of plasma density and confinement [2]. The toroidal geometry tokamak concept is presently the leading scheme for confining plasma by magnetic fields. In tokamak operation, auxiliary heating is often accomplished by radio-frequency (RF) waves. Heating by RF waves in the ion cyclotron range of frequencies (ICRF), also referred to as ion cyclotron heating (ICH), is one of the common methods [3]. However, a challenge in ICH is that the antenna needs to face the plasma in the scrape-off layer (SOL) — the region where the flux surfaces intersect with solid structures in a tokamak. In this circumstance, even if the antenna is placed in a low plasma density and low temperature area, the antenna, the metal structures in its vicinity, and the first wall can be seriously damaged due to the effect of "RF sheaths."

RF sheath formation is known as one of the most important nonlinear effects in the edge plasma of ICH fusion devices [4–6]. Particularly, sheaths on the antenna surface and nearby material boundaries, such as limiters, are referred to as near-field sheaths. A strong candidate for the appearance of RF sheaths in experiments, and a fundamental, well-investigated physical mechanism is the generation of the parasitic slow wave (SW), which has a large $E_\parallel$ component (electric field component parallel to the background magnetic field) driven by the current straps. Due to the presence of the SW with a large-amplitude $E_\parallel$ field, more electrons are expelled from the plasma into the boundary surface when the electric field points into the plasma than heavier ions are expelled by the electric field in the opposite direction, leading to the development of the net positive direct-current voltage, namely, the "rectified" sheath potential to maintain charge ambipolarity [7]. When the current source is large, the rectified sheath potential can reach the order of kV and has important consequences. As a result of the increased sheath potential, ions are significantly accelerated in the close vicinity of wall material, causing enhanced sputtering, impurity generation, and power dissipation [8–13].

The spatial distribution of the sheath potential can be estimated in the vacuum approximation (neglecting plasma dielectric effects) by integrating $E_\parallel$ along each field line between the contact points with the bounding surface, e.g., the antenna. Here, $E_\parallel$ is obtained from the RF wave solution in a vacuum. This approximation proved useful in studying qualitative trends (e.g., see Ref. [8]) and is still commonly used today for antenna design studies and experimental data analysis (e.g., see Ref. [13]). However, in future long-pulse, high power tokamaks, such as International Thermonuclear Ex-

perimental Reactor (ITER), the need for sheath control will be greater, and quantitative methods of calculating the sheath potential (including plasma effects) will be needed. Note that the plasma dielectric also controls the direction of wave propagation and thus the contact of the RF waves with the boundary [14].

Because the magnitude of the RF sheath potential can be sensitive to complex details (in both the geometry and RF wave physics), a numerical approach is required for quantitative results. Typically, a numerical simulation must cover the main plasma (the edge and/or core plasma in a tokamak), where characteristic lengths are several orders of magnitude greater than a typical sheath width. In order to avoid excessive computational costs, it is therefore advantageous to develop a numerical scheme which does not require numerical resolution of the sheath itself. There have been several previous approaches to this problem [15, 16] which incorporated the Godyak-Lieberman sheath models [17, 18]. For example, RF sheath potentials pertaining to plasma processing problems in two-dimensional (2D) domains were obtained in Ref. [15] by incorporating a sub-grid sheath model through an effective local dielectric.

Another approach that approximately treats the sheath effects is to introduce the "sheath boundary condition (BC)" proposed in Refs. [19, 20]. The idea is that essential sheath effects on the plasma are captured through the boundary condition. In this approach, the field quantities in the sheath are not referenced directly in the final form of the boundary condition because they have been eliminated analytically. The derivation of the sheath BC is based on the assumption that the sheath is effectively a vacuum region characterized by a capacitance. Even in this approximation, the sheath BC captures the most important physics that happens in the sheath, that is, the rapid variation of the very large dielectric tensor component $\varepsilon_{\|}$ (later shown in Eq. (3)) in the sheath region. In this paper we use the original implementation of the sheath BC in the frequency domain; its use in the time-domain is also being explored in Ref. [21].

Our objective in this paper is to present a finite element procedure in which RF sheath-plasma interactions in the ICRF are taken into account through the sheath BC. Our approach significantly extends previous attempts along these lines [22] by allowing for truly self-consistent calculations; that is, the sheath width is determined in conjunction with the electric field strength on the sheath surface, which satisfies Maxwell's equations and the sheath BC simultaneously. Full plasma dielectric effects are retained in both

the wave propagation and sheath BC. In addition, the proposed method is amenable to the problem that has a spatially complicated geometry owing to finite element discretization.

In the present paper, we will explicitly consider the effect of RF sheaths on wall surfaces near the antenna rather than on the antenna surface itself. The method proposed here is fundamentally independent of these details; however, a realistic antenna surface is three-dimensional and geometrically complex, and thus inappropriate for an initial analysis focused on verification.

The paper is organized as follows: in Section 2 we describe the equations and expressions used for the present numerical analysis of RF sheath-plasma interactions. Section 3 presents the finite element procedure in detail, and its validity is verified by comparison with an analytical solution in the 1D closed domain and the result of the local dispersion relation in Section 4. The variation of sheath potential with antenna current is also investigated based on the parameters for Alcator C-Mod (a tokamak at the MIT Plasma Science and Fusion Center). Further, a numerical example in a 2D domain whose scale is equivalent to the Alcator C-Mod tokamak is presented in Section 5. Lastly, conclusions of the present work are described in Section 6.

2. Problem formulation for RF sheath-plasma interactions

This section summarizes the equations that govern the behavior of plasma waves in the SOL and the interaction between the waves and the sheaths on metal surfaces. These equations and boundary conditions are directly employed in the present finite element numerical analyses. The geometry considered here is shown in Fig. 1; this is a simplified schematic of the tokamak poloidal cross-section in the vicinity of the limiter, assuming that the magnetic field lines intersect with a metal surface and thereby the sheath is formed. All the analyses in this study will be conducted using a cold plasma model, which is typically valid due to low plasma temperatures (~ 10 eV). Also, we assume that only deuterium is considered as an ion species, so that the ion mass is $m_{\mathrm{i}} = 3.3436 \times 10^{-27}$ kg.

The governing equation for plasma waves in the SOL is a combined form of Maxwell's equations described as

$$\nabla \times \nabla \times \boldsymbol{E} - \frac{\omega^2}{c^2} \boldsymbol{\varepsilon} \cdot \boldsymbol{E} - i\omega\mu_0 \boldsymbol{J}_{\mathrm{ext}} = \boldsymbol{0}, \tag{1}$$

where the electric field $\boldsymbol{E}$ and the external current $\boldsymbol{J}_{\mathrm{ext}}$ vary on the RF time scale. Here, ω is the applied angular velocity, and c is the speed of light,

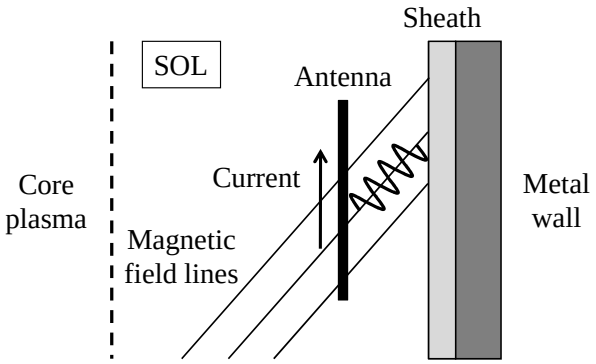

Figure 1: Illustration of a tokamak poloidal cross-section in the vicinity of the limiter.

having a relation with the dielectric constant ε_0 and the permeability μ_0 in vacuum, which is expressed as $c^2 = (\varepsilon_0 \mu_0)^{-1}$. The dielectric tensor $\boldsymbol{\varepsilon}$ is given by

$$\boldsymbol{\varepsilon} = (\boldsymbol{I} - \boldsymbol{bb})\,\varepsilon_\perp + \boldsymbol{bb}\varepsilon_\parallel + i\boldsymbol{b} \times \boldsymbol{I}\varepsilon_\times, \tag{2}$$

where $\boldsymbol{I}$ is the unit tensor, and $\boldsymbol{b}$ is the unit vector along the background magnetic field $\boldsymbol{B}_0$ ($\boldsymbol{b} = \boldsymbol{B}_0/|\boldsymbol{B}_0|$); the subscript 0 denotes an equilibrium quantity. Here the coefficients $\varepsilon_\perp$, $\varepsilon_\parallel$, and $\varepsilon_\times$ are expressed as follows:

$$\varepsilon_\perp = 1 - \sum_j \frac{\omega_{\mathrm{p}j}^2}{\omega^2 - \Omega_j^2}, \quad \varepsilon_\parallel = 1 - \sum_j \frac{\omega_{\mathrm{p}j}^2}{\omega^2}, \quad \varepsilon_\times = \sum_j \frac{\omega_{\mathrm{p}j}^2 \Omega_j}{\omega\left(\omega^2 - \Omega_j^2\right)}, \tag{3}$$

where $\omega_{\mathrm{p}j}$ is the plasma frequency defined as $\omega_{\mathrm{p}j} = (n_{j0}e^2/\varepsilon_0 m_j)^{1/2}$, and $\Omega_j = q_j B_0/m_j$; q_j is the electric charge ($|q_j| = e$), and the subscript j indicates two-species particles, i.e., an ion (i) or an electron (e). Throughout this study, we assume that quasi-neutrality in the plasma is retained, i.e., $n_{\mathrm{e}0} = n_{\mathrm{i}0} = n_0$.

Due to the difference in thermal velocity between electrons and ions at a conducting surface, a potential barrier is formed to confine the electrons and restore charge ambipolarity in the plasma. The layer in which the potential drop occurs is called the thermal (Bohm) sheath, and a condition for ion-rich sheath formation is that $\vartheta \gtrsim (m_{\mathrm{e}}/m_{\mathrm{i}})^{1/2}$, where ϑ is the contact angle between the magnetic field line and the sheath. On the other hand, when RF waves with large electric-field strength approach the wall, the electrons are further accelerated along the field lines, yielding higher voltages inside

the sheath compared to the thermal sheath potential. This RF driven sheath further accelerates ions, enhancing sputtering as a result.

In the present numerical analysis, the sheath effect is taken into account by means of the sheath BC, which is written as follows:

$$\boldsymbol{E}_{\mathrm{t}} = \nabla_{\mathrm{t}} \left(\frac{\Delta_{\mathrm{sh}}}{\varepsilon_{\mathrm{sh}}} D_{\mathrm{n}} \right). \tag{4}$$

Here, Δ_{sh} is the time-averaged sheath width, $\varepsilon_{\mathrm{sh}}$ is the dielectric constant in the sheath (in this study we assume that $\varepsilon_{\mathrm{sh}} = \varepsilon_0$), D_{n} $(= \boldsymbol{s} \cdot (\varepsilon_0 \boldsymbol{\varepsilon} \cdot \boldsymbol{E}))$ is the normal component of the electric displacement (and $\boldsymbol{s}$ in the definition is the unit normal vector pointing to the plasma), and the subscript t denotes the tangential component to the boundary. The sheath BC is derived by (1) assuming that the sheath region is approximated as vacuum, (2) the conditions of continuity of $\boldsymbol{E}_{\mathrm{t}}$ and D_{n} at the sheath-plasma interface, and (3) the electrostatic approximation in vacuum [19, 20]. The above boundary condition is described only with the quantities on the plasma side, which makes it unnecessary to resolve the narrow sheath region in numerical analysis. Further, an important physical observation is that for $\Delta_{\mathrm{sh}} \to 0$ the sheath BC naturally reduces to the conducting-wall BC, $\boldsymbol{E}_{\mathrm{t}} = \boldsymbol{0}$.

Assuming that the sheath width satisfies the Child-Langmuir law [23, 24], a useful approximate expression for the sheath width can be written as follows:

$$\Delta_{\mathrm{sh}} = \left(\frac{e C_{\mathrm{sh}}}{\varepsilon_{\mathrm{sh}} T_{\mathrm{e}}} |D_{\mathrm{n}}| \right)^3 \lambda_{\mathrm{De}}^4 + C_{\mathrm{th}} \lambda_{\mathrm{De}}, \tag{5}$$

where C_{sh} is an order-unity constant giving the rectification factor [7], T_{e} is the electron temperature, λ_{De} is the electron Debye length defined as $\lambda_{\mathrm{De}} = (\varepsilon_0 T_{\mathrm{e}} / n_{\mathrm{e}0} e^2)^{1/2}$. The coefficient C_{th} is given by

$$C_{\mathrm{th}} = \begin{cases} 0 & \text{for } \vartheta \le (m_{\mathrm{e}}/m_{\mathrm{i}})^{1/2} \\ \left\{ \ln \left[\left(\frac{m_{\mathrm{i}}}{m_{\mathrm{e}}} \right)^{1/2} \sin\vartheta \right] \right\}^{3/4} & \text{for } \vartheta > (m_{\mathrm{e}}/m_{\mathrm{i}})^{1/2}, \end{cases} \tag{6}$$

where ϑ is the angle between the magnetic field line and the sheath surface, defined such that $\vartheta = 0$ ($\vartheta = \pi/2$) describes field lines parallel (normal) to the surface. The definition in Eq. (6) is consistent with the transition from the ion-rich sheath ($\vartheta > (m_{\mathrm{e}}/m_{\mathrm{i}})^{1/2}$) to electron-rich sheath ($\vartheta < (m_{\mathrm{e}}/m_{\mathrm{i}})^{1/2}$),

whose physics is not considered here. This definition precludes negative values from the logarithm. The first term in Eq. (5), which is nonlinear in the unknown electric field, is dominant for strong RF sheaths, and the Bohm sheath contribution is introduced as a correction term in the second term. Eq. (5) is strictly valid for $eV_{\rm sh}/T_{\rm e} \gg 1$ and $eV_{\rm sh}/T_{\rm e} \ll 1$, where $V_{\rm sh}$ is the instantaneous sheath voltage defined by

$$V_{\rm sh} \equiv \left| \int E_{\rm n}^{\rm (sh)} d\upsilon \right| \simeq \Delta_{\rm sh} \left| E_{\rm n}^{\rm (sh)} \right| = \Delta_{\rm sh} \left| \frac{D_{\rm n}^{\rm (pl)}}{\varepsilon_{\rm sh}} \right|, \tag{7}$$

where the superscripts sh and pl denote the quantities in the sheath and plasma, respectively, and υ corresponds to the direction perpendicular to the sheath surface. In intermediate cases, $eV_{\rm sh}/T_{\rm e} \sim 1$, Eq. (5) provides a convenient and approximate interpolation. The corresponding rectified sheath potential can be obtained from the Child-Langmuir law as follows:

$$V_0 = \frac{T_{\rm e}}{e} \left(\frac{\Delta_{\rm sh}}{\lambda_{\rm De}} \right)^{4/3}, \tag{8}$$

which approaches $C_{\rm sh} V_{\rm sh}$ for $eV_{\rm sh}/T_{\rm e} \gg 1$ and $V_{\rm B}$ for $eV_{\rm sh}/T_{\rm e} \ll 1$, where $V_{\rm B}$ is the Bohm sheath potential.

Although there is no clear boundary between the hot core plasma and the cold plasma in the SOL, the core plasma needs to be excluded from the calculation domain since obviously the cold plasma formulation cannot be applied to this high temperature plasma. In cases of practical interest for tokamak heating, it is desirable that most of the RF waves that enter the core plasma are absorbed there. As far as studying the RF sheath-plasma interactions in the SOL is concerned, it does not matter how this absorption occurs, so we can use an artificial absorption condition at the boundary of the edge and core regions as a numerical device to implement an outgoing wave condition. The easiest way is to introduce a damping layer in the vicinity of the core-edge plasma boundary. This can be achieved by defining the electron mass as $m_{\rm e}\left(1 + i\nu/\omega\right)$ and choosing the artificial collision frequency ν to decrease exponentially from the core-edge plasma boundary. As an example, ν is described in the following equation for a slab geometry:

$$\nu = \nu_0 \exp\left(-\frac{x - x_{\rm abs}}{\lambda_\nu} \right), \tag{9}$$

where the domain is $x > x_{\rm abs}$, ν_0 is the maximum artificial frequency, $x_{\rm abs}$ is the position of the core-side boundary of the plasma, and λ_ν represents the length of the damping layer. The choice of the values for ν_0 and λ_ν depends on the calculation condition and requires some numerical experimentation. With this procedure, the actual boundary condition on the core side is not important, so that we can impose the conducting-wall BC, $\boldsymbol{E}_{\rm t} = \boldsymbol{0}$, for example. This condition, together with the damping layer, is called the "absorbing BC" in later numerical analyses.

3. Finite element discretizations

In this section, the discretization procedure for the present differential formulation is described with the assumption that the calculation domain (edge plasma in the poloidal plane of a tokamak) is bounded by the sheath and absorbing BCs. We first aim at obtaining a set of coupled equations for the unknown nodal values of the electric field components in the Cartesian coordinate system; in Section 3.1, we consider the equations in the volume, and subsequently in Section 3.3 focus on the sheath BC. Then, we apply a Newton-Raphson method to the resultant nonlinear system of discretized equations in order to obtain a converged solution. The developed finite element code is named "rfSOL (integrated code for RF sheath-plasma interactions with a realistic SOL geometry)," and its validity will be verified with several test problems in 1D domains in the next section.

3.1. Discretization of Maxwell's equation

The present numerical scheme is constructed based on the weighted residual method [25]. First, forming the inner product of Eq. (1) with the weight function $\boldsymbol{W}$, and then integrating it over the calculation domain Ω yields

$$\int_\Omega \boldsymbol{W} \cdot \left(\nabla \times \nabla \times \boldsymbol{E} - \frac{\omega^2}{c^2} \boldsymbol{\varepsilon} \cdot \boldsymbol{E} - i\omega\mu_0 \boldsymbol{J}_{\rm ext} \right) d\Omega = 0. \tag{10}$$

The first term on the left-hand side of Eq. (10) is rewritten as follows:

$$T_1 = \int_\Omega \nabla \times \boldsymbol{W} \cdot \nabla \times \boldsymbol{E}\, d\Omega - \int_\Gamma \hat{\boldsymbol{n}} \times \boldsymbol{W} \cdot \nabla \times \boldsymbol{E}\, d\Gamma, \tag{11}$$

where Γ represents the boundary of the domain Ω, and $\hat{\boldsymbol{n}}$ is the outward-pointing unit normal vector on Γ. Here, Gauss's theorem is employed to

obtain the boundary integral term. Since the sheath and absorbing BCs are regarded as Dirichlet boundary conditions and imposed on the tangential components of the electric field at the boundary, the weight function $\boldsymbol{W}$ is chosen such that its tangential components are zero ($\boldsymbol{W}_{\mathrm{t}} = \boldsymbol{0}$) on the boundary surface. Then, the boundary integral term in Eq. (11) is omitted due to the fact that $\hat{\boldsymbol{n}} \times \boldsymbol{W} = \boldsymbol{0}$. Consequently, the weak form of Maxwell's equation for this analysis is given by

$$\int_{\Omega} \left(\nabla \times \boldsymbol{W} \cdot \nabla \times \boldsymbol{E} - \frac{\omega^2}{c^2} \boldsymbol{W} \cdot \boldsymbol{\varepsilon} \cdot \boldsymbol{E} - i\omega\mu_0 \boldsymbol{W} \cdot \boldsymbol{J}_{\mathrm{ext}} \right) d\Omega = 0. \tag{12}$$

In order to spatially discretize Eq. (12) in the x-y plane, the calculation domain is divided into nine-node grid elements, and then the weight function and electric field are defined based on the standard Galerkin approach as follows:

$$\boldsymbol{W} = \hat{\boldsymbol{W}}_i N_i (x, y) \, \mathrm{e}^{-ik_z z} = \tilde{N}_i \hat{\boldsymbol{W}}_i, \tag{13}$$

$$\boldsymbol{E} = \hat{\boldsymbol{E}}_j N_j (x, y) \, \mathrm{e}^{i(k_z z - \omega t)} = \tilde{N}_j \hat{\boldsymbol{E}}_j \mathrm{e}^{-i\omega t}, \tag{14}$$

where N_i and N_j are the piecewise biquadratic interpolation functions, $\hat{\boldsymbol{W}}_i$ and $\hat{\boldsymbol{E}}_j$ are the nodal vectors, and the subscripts i and j denote the global node number. The summation convention applies to the subscripts i and j.

Substituting Eq. (13) into Eq. (12), we obtain

$$\hat{\boldsymbol{W}}_i \cdot \int_{\Omega} \left(\nabla \times \boldsymbol{E} \times \nabla \tilde{N}_i - \frac{\omega^2}{c^2} \tilde{N}_i \boldsymbol{\varepsilon} \cdot \boldsymbol{E} - i\omega\mu_0 \tilde{N}_i \boldsymbol{J}_{\mathrm{ext}} \right) d\Omega = 0. \tag{15}$$

Here, we assume that the external current is expressed as

$$\boldsymbol{J}_{\mathrm{ext}} = J_{\mathrm{ant}} \mathrm{e}^{i(k_z z - \omega t)} \boldsymbol{e}_y \tag{16}$$

for simplicity (where $\boldsymbol{e}_y$ is the unit vector in the y direction; the same shall apply to $\boldsymbol{e}_x$ and $\boldsymbol{e}_z$) and the dielectric tensor is interpolated as $\boldsymbol{\varepsilon} = N_k \boldsymbol{\varepsilon}_k$ using its nodal values $\boldsymbol{\varepsilon}_k$. Then, the requirement that Eq. (15) needs to be satisfied for arbitrary weight functions leads to the following equation in the calculation domain:

$$\boldsymbol{F} = \boldsymbol{R}, \tag{17}$$

where

$$\boldsymbol{F} = \int_{\Omega} \left[\nabla \times \left(\tilde{N}_j \hat{\boldsymbol{E}}_j \right) \times \nabla \tilde{N}_i - \frac{\omega^2}{c^2} N_i N_j N_k \boldsymbol{\varepsilon}_k \cdot \hat{\boldsymbol{E}}_j \right] d\Omega, \tag{18}$$

$$\boldsymbol{R} = i\omega\mu_0 \boldsymbol{e}_y \int_{\Omega} N_i J_{\mathrm{ant}} d\Omega. \tag{19}$$

Here, the Jacobian and the components of the cofactor matrix in each grid element are evaluated at the centroid of the element. Owing to this approximation, all the integrals are calculated analytically, which can lead to significant speed-up of the scheme (however, to retain accuracy of this approach, a sufficient number of grid points can sometimes be required to avoid large grid distortion). The detailed calculations of the integrals are summarized in Ref. [26]. The discretization of the term including the external current will be described in the next subsection.

3.2. Discretization of the antenna current

In this study, for simplicity, the external (antenna) current is modeled as a sheet current, with a delta function in, i.e., $J_{\mathrm{ant}} = K(y)\,\delta(x - x_{\mathrm{ant}})$; here we assume that the current strap is located at $x = x_{\mathrm{ant}}$. Also, we assume that the antenna is always located along element borders. Then the integral in Eq. (19) is calculated as follows:

$$\int_{\Omega} N_i J_{\mathrm{ant}} d\Omega = \int_{l} N_i^{\mathrm{A}} N_j^{\mathrm{A}} K_j dl, \tag{20}$$

where l represents the 1D coordinate along the direction of the antenna current, and the subscripts i and j denote the global node number of the nodes located on the current strap (see Fig. 2). Here, the surface current K is interpolated as $K = N_j^{\mathrm{A}} K_j$ using its nodal values K_j. The shape function N_j^{A} is the piecewise quadratic interpolation function which can be defined in a 1D grid element on the current strap.

3.3. Discretization of the sheath boundary condition

The sheath BC described in Eq. (4) can be discretized by employing the 1D finite element method when we consider a problem in the 2D space. First, forming the inner product of Eq. (4) with the weight function $\boldsymbol{W}^{\mathrm{S}}$, and then integrating it over the sheath region Γ^{S} yields

$$\int_{\Gamma^{\mathrm{S}}} \boldsymbol{W}^{\mathrm{S}} \cdot \left[\boldsymbol{E}_{\mathrm{t}} - \nabla_{\mathrm{t}} \left(\Delta_{\mathrm{sh}} \kappa \right) \right] d\Gamma^{\mathrm{S}} = 0, \tag{21}$$

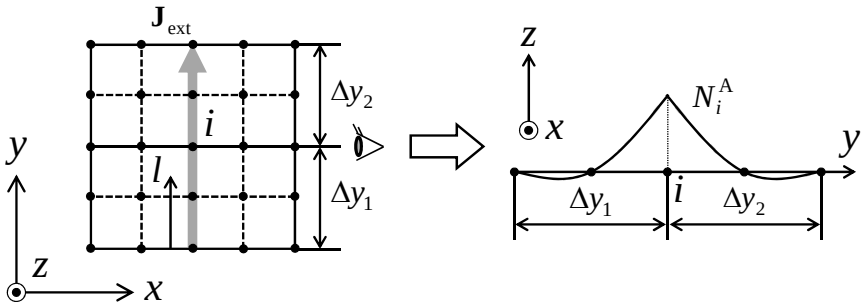

Figure 2: The interpolation function N_i^{A} defined along the antenna current.

where $\kappa = \boldsymbol{s}\cdot(\boldsymbol{\varepsilon}\cdot\boldsymbol{E})$. Let us next define the weight function and electric field as

$$\boldsymbol{W}^{\mathrm{S}} = \hat{\boldsymbol{W}}_i^{\mathrm{S}} N_i^{\mathrm{S}}(\tau)\,\mathrm{e}^{-ik_z z} = \tilde{N}_i^{\mathrm{S}}\hat{\boldsymbol{W}}_i^{\mathrm{S}}, \tag{22}$$

$$\boldsymbol{E} = \hat{\boldsymbol{E}}_j^{\mathrm{S}} N_j^{\mathrm{S}}(\tau)\,\mathrm{e}^{i(k_z z-\omega t)}, \tag{23}$$

where N_i^{S} and N_j^{S} are the piecewise quadratic interpolation functions with respect to τ (the tangential direction with respect to the sheath surface), and the subscripts i and j denote the global node number on Γ^{S}. Here the summation convention applies to the subscripts i and j, and the superscript S is attached to explicitly show that the quantity is positioned on Γ^{S}. The shape function N_i^{S} or N_j^{S} can be locally defined in a 1D grid element on the sheath. Considering that Eq. (21) needs to be satisfied for arbitrary weight functions, one gets

$$\int_{\Gamma^{\mathrm{S}}} \tilde{N}_i^{\mathrm{S}}\left[\boldsymbol{E}_{\mathrm{t}} - \nabla_{\mathrm{t}}\left(\Delta_{\mathrm{sh}}\kappa\right)\right] d\Gamma^{\mathrm{S}} = \boldsymbol{0}. \tag{24}$$

The τ component of the integral equation (24) is written as

$$\int_{\Gamma^{\mathrm{S}}} \tilde{N}_i^{\mathrm{S}}\left[E_\tau - \frac{\partial}{\partial\tau}\left(\Delta_{\mathrm{sh}}\kappa\right)\right] d\Gamma^{\mathrm{S}} = 0. \tag{25}$$

Now, let us make the following approximation for the derivative of $\Delta_{\mathrm{sh}}\kappa$:

$$\begin{aligned}\frac{\partial}{\partial\tau}\left(\Delta_{\mathrm{sh}}\kappa\right) \simeq &\left(\left\langle\frac{d\Delta_{\mathrm{sh}}}{d\tau}\right\rangle_{\mathrm{e}}\langle\boldsymbol{s}\rangle_{\mathrm{e}} + \langle\Delta_{\mathrm{sh}}\rangle_{\mathrm{e}}\left\langle\frac{d\boldsymbol{s}}{d\tau}\right\rangle_{\mathrm{e}}\right)\cdot(\boldsymbol{\varepsilon}\cdot\boldsymbol{E}) \\ &+ \langle\Delta_{\mathrm{sh}}\rangle_{\mathrm{e}}\langle\boldsymbol{s}\rangle_{\mathrm{e}}\cdot\frac{\partial}{\partial\tau}\left(\boldsymbol{\varepsilon}\cdot\boldsymbol{E}\right).\end{aligned} \tag{26}$$

Here, the variables surrounded by angle brackets with the subscript e represent the element-averaged quantities (see Appendix A). Eq. (26) is an important approximation which simplifies the discretization of the nonlinear sheath BC (recall that $\Delta_{\rm sh} \propto |D_{\rm n}|^3$ in the RF-dominated limit). Assuming that the dielectric tensor on $\Gamma^{\rm S}$ is interpolated as $\boldsymbol{\varepsilon} = N_k^{\rm S} \boldsymbol{\varepsilon}_k^{\rm S}$ using its nodal values $\boldsymbol{\varepsilon}_k^{\rm S}$, and substituting Eqs. (23) and (26) into Eq. (25), we obtain

$$\begin{aligned} G_{\tau i} \equiv \sum_m \Bigg\{ & \left[N_i^{\rm S} N_j^{\rm S} \right] \hat{E}_{\tau j}^{\rm S} \\ & - \Bigg[\left(\left\langle \frac{d\Delta_{\rm sh}}{d\tau} \right\rangle_{{\rm e}(m)} \langle \boldsymbol{s} \rangle_{{\rm e}(m)} + \langle \Delta_{\rm sh} \rangle_{{\rm e}(m)} \left\langle \frac{d\boldsymbol{s}}{d\tau} \right\rangle_{{\rm e}(m)} \right) \left[N_i^{\rm S} N_j^{\rm S} N_k^{\rm S} \right] \\ & + \langle \Delta_{\rm sh} \rangle_{{\rm e}(m)} \langle \boldsymbol{s} \rangle_{{\rm e}(m)} \left[N_i^{\rm S} \check{N}_j^{\rm S} \check{N}_k^{\rm S} \right] \Bigg] \cdot \left(\boldsymbol{\varepsilon}_k^{\rm S} \cdot \hat{\boldsymbol{E}}_j^{\rm S} \right) \Bigg\} = 0, \end{aligned} \tag{27}$$

with

$$\begin{aligned} & \left[N_i^{\rm S} N_j^{\rm S} \right] \equiv \int_{\Gamma^{\rm S}_{{\rm e}(m)}} N_i^{\rm S} N_j^{\rm S} d\Gamma^{\rm S}, \quad \left[N_i^{\rm S} N_j^{\rm S} N_k^{\rm S} \right] \equiv \int_{\Gamma^{\rm S}_{{\rm e}(m)}} N_i^{\rm S} N_j^{\rm S} N_k^{\rm S} d\Gamma^{\rm S}, \\ & \left[N_i^{\rm S} \check{N}_j^{\rm S} \check{N}_k^{\rm S} \right] \equiv \int_{\Gamma^{\rm S}_{{\rm e}(m)}} N_i^{\rm S} \frac{dN_j^{\rm S}}{d\tau} N_k^{\rm S} d\Gamma^{\rm S} + \int_{\Gamma^{\rm S}_{{\rm e}(m)}} N_i^{\rm S} N_j^{\rm S} \frac{dN_k^{\rm S}}{d\tau} d\Gamma^{\rm S}, \end{aligned} \tag{28}$$

where m represents 1D grid elements (or a 1D grid element) which include(s) the node i. The quantities with the subscript e (m) are nonzero only in the grid element m. The calculations of the integrals in Eq. (28) are summarized in Ref. [26]. The quantity $\hat{E}_{\tau j}^{\rm S}$ needs to be expressed using $\hat{E}_{xj}^{\rm S}$ and $\hat{E}_{yj}^{\rm S}$ with use of the following relation:

$$\hat{E}_{\tau j}^{\rm S} = \boldsymbol{e}_x \cdot \boldsymbol{e}_{\tau j} \hat{E}_{xj}^{\rm S} + \boldsymbol{e}_y \cdot \boldsymbol{e}_{\tau j} \hat{E}_{yj}^{\rm S}, \tag{29}$$

where $\boldsymbol{e}_{\tau j}$ is the unit vector in the τ direction at the node j, which can be obtained by applying the nodal-average method to the grid edges on the boundary, for example.

The z component of Eq. (24) is written as

$$\int_{\Gamma^{\rm S}} \tilde{N}_i^{\rm S} \left(E_z - i k_z \Delta_{\rm sh} \kappa \right) d\Gamma^{\rm S} = 0, \tag{30}$$

considering that $\kappa \propto {\rm e}^{ik_z z}$. Then the corresponding discretized equation is

given by

$$G_{zi} \equiv \sum_m \Big[\left[N_i^{\mathrm{S}} N_j^{\mathrm{S}} \right] \hat{E}_{zj}^{\mathrm{S}} \\ -ik_z \left\langle \Delta_{\mathrm{sh}} \right\rangle_{\mathrm{e}(m)} \left\langle \boldsymbol{s} \right\rangle_{\mathrm{e}(m)} \left[N_i^{\mathrm{S}} N_j^{\mathrm{S}} N_k^{\mathrm{S}} \right] \cdot \left(\boldsymbol{\varepsilon}_k^{\mathrm{S}} \cdot \hat{\boldsymbol{E}}_j^{\mathrm{S}} \right) \Big] = 0 \tag{31}$$

using the approximations that $\Delta_{\mathrm{sh}} \simeq \left\langle \Delta_{\mathrm{sh}} \right\rangle_{\mathrm{e}(m)}$ and $\boldsymbol{s} \simeq \left\langle \boldsymbol{s} \right\rangle_{\mathrm{e}(m)}$.

The resultant nonlinear system of discretized equations can be solved by employing the Newton-Raphson method, which is one of the most frequently used iteration schemes. (A number of related methods can be seen in Ref. [27].) The procedure is described in Appendix B. In this study, the system of linear equations at each Newton-Raphson iteration is computed by employing MUMPS (MUltifrontal Massively Parallel Solver) on the Franklin Cray XT4 computer system at the National Energy Research Scientific Computing Center (NERSC).

4. Code verification in 1D geometry

In order to verify the developed numerical scheme named "rfSOL," first, in this section we derive an analytical solution for the plasma wave driven by the antenna current in the 1D geometry subject to the sheath BC at both ends, and compare the numerical result with the corresponding analytical result. Then the rfSOL code is applied to the problems that include a varying density profile and an absorbing layer, and propagating SW-sheath interactions are investigated by taking account of the change in sheath width. Particular attention is focused on the limit where the sheath width approaches infinity from a mathematical standpoint, since this is an extreme limit of the new regime made assessable by the present code.

4.1. Analytical solution for constant n_0 and $\boldsymbol{B}_0$

The calculation domain considered here is shown in Fig. 3; a constant-density plasma is filled in a waveguide which is assumed to be infinitely long in the y and z directions. The background magnetic field is also assumed to be constant in magnitude and pointed purely in the x direction. The sheath BC is imposed at both $x = x_{\mathrm{L}}$ and $x = x_{\mathrm{R}}$. The wavenumber components k_y and k_z are fixed (imposed), and the antenna current density is given by

$$\boldsymbol{J}_{\mathrm{ext}} = K\delta\left(x - x_{\mathrm{ant}}\right) \mathrm{e}^{i(k_y y + k_z z - \omega t)} \boldsymbol{e}_y = \boldsymbol{K}\delta\left(x - x_{\mathrm{ant}}\right),$$

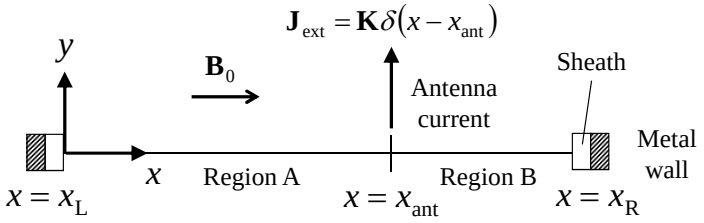

Figure 3: 1D calculation model for the derivation of the analytical solution.

where K is constant.

The derivation starts from a single vector equation for $\boldsymbol{E}$ shown in Eq. (1). From Eq. (2) we can write the dielectric tensor components as

$$\boldsymbol{\varepsilon} = \begin{pmatrix} \varepsilon_{xx} & 0 & 0 \\ 0 & \varepsilon_{yy} & \varepsilon_{yz} \\ 0 & \varepsilon_{zy} & \varepsilon_{zz} \end{pmatrix} \tag{32}$$

due to the assumption that $b_y = b_z = 0$. Now, let us look for a solution to Eq. (1) in the form $\boldsymbol{E} = \hat{\boldsymbol{E}} \mathrm{e}^{i(k_x x + k_y y + k_z z - \omega t)}$. Then, we obtain the dispersion relation that forms a quadratic equation in terms of k_x^2. When the domain is divided by the presence of the external surface current, the general solutions for the electric field in region A and region B in Fig. 3 are, respectively, written as

$$\boldsymbol{E}_{\mathrm{A}} = \left(\sum_{j=1}^{4} C_{\mathrm{A}j} \tilde{\boldsymbol{E}}_j \mathrm{e}^{ik_{xj}x} \right) \mathrm{e}^{i(k_y y + k_z z - \omega t)}, \tag{33}$$

$$\boldsymbol{E}_{\mathrm{B}} = \left(\sum_{j=1}^{4} C_{\mathrm{B}j} \tilde{\boldsymbol{E}}_j \mathrm{e}^{ik_{xj}x} \right) \mathrm{e}^{i(k_y y + k_z z - \omega t)}, \tag{34}$$

where $C_{\mathrm{A}1}, \ldots, C_{\mathrm{A}4}$ and $C_{\mathrm{B}1}, \ldots, C_{\mathrm{B}4}$ are constants to be determined, and $\tilde{\boldsymbol{E}}_j$ is the polarization eigenvector corresponding to k_{xj}. The corresponding expressions for the magnetic field are calculated by Faraday's law.

Since the magnetic field line intersects at a right angle with the walls, the sheath must be present at both ends, which yields the following four conditions:

$$\begin{aligned} \boldsymbol{E}_{\mathrm{A}t}|_{x=x_{\mathrm{L}}} &= i\boldsymbol{k}_{\mathrm{t}} \left[\left(\alpha_{\mathrm{sh}} \left| \varepsilon_{xx} E_x \right|^3 + \beta_{\mathrm{sh}} \right) \varepsilon_{xx} E_x \right] \big|_{x=x_{\mathrm{L}}}, \\ \boldsymbol{E}_{\mathrm{B}t}|_{x=x_{\mathrm{R}}} &= -i\boldsymbol{k}_{\mathrm{t}} \left[\left(\alpha_{\mathrm{sh}} \left| \varepsilon_{xx} E_x \right|^3 + \beta_{\mathrm{sh}} \right) \varepsilon_{xx} E_x \right] \big|_{x=x_{\mathrm{R}}}, \end{aligned} \tag{35}$$

where

$$\alpha_{\mathrm{sh}} = \left(\frac{eC_{\mathrm{sh}}}{T_{\mathrm{e}}}\right)^3 \lambda_{\mathrm{De}}^4, \quad \beta_{\mathrm{sh}} = C_{\mathrm{th}}\lambda_{\mathrm{De}}, \\ \boldsymbol{k}_{\mathrm{t}} = k_y \boldsymbol{e}_y + k_z \boldsymbol{e}_z. \tag{36}$$

Note that Eq. (35) is a nonlinear constraint for the electric field. This nonlinearity comes about from imposing the Child-Langmuir constraint (see Eq. (8)). At the position where the surface current is present ($x = x_{\mathrm{ant}}$), one has to consider the jump conditions in both the electric and magnetic fields, which are given by

$$E_{\mathrm{A}y}|_{x=x_{\mathrm{ant}}} = E_{\mathrm{B}y}|_{x=x_{\mathrm{ant}}}, \quad E_{\mathrm{A}z}|_{x=x_{\mathrm{ant}}} = E_{\mathrm{B}z}|_{x=x_{\mathrm{ant}}}, \\ B_{\mathrm{A}y}|_{x=x_{\mathrm{ant}}} = B_{\mathrm{B}y}|_{x=x_{\mathrm{ant}}}, \quad B_{\mathrm{A}z} - B_{\mathrm{B}z}|_{x=x_{\mathrm{ant}}} = \mu_0 K \mathrm{e}^{i(k_y y + k_z z - \omega t)}. \tag{37}$$

Consequently, one finds that the problem can be analytically solved since eight unknowns are calculated with the same number of equations. Due to the nonlinearity in the sheath BC, one has to iteratively calculate the system of equations to obtain the constants $C_{\mathrm{A}j}$ and $C_{\mathrm{B}j}$, for example, using the Newton-Raphson method.

4.2. Comparison between the analytical and numerical solutions

First of all, a numerical result obtained with the 1D rfSOL code, which is straightforwardly constructed by converting $\partial/\partial y$ to ik_y in Section 3, is compared with the result given by the analytical solution. Based on Fig. 3, the calculation domain is defined such that $x_{\mathrm{L}} = 0$ m, $x_{\mathrm{ant}} = 3.5$ m, and $x_{\mathrm{R}} = 5$ m. The plasma density and background magnetic field are assumed to be constant; $n_0 = 2 \times 10^{17}$ m^{-3} and $B_0 = 5.4$ T. The other parameters fixed in this analysis are $f = 80$ MHz, $T_{\mathrm{e}} = 10$ eV, $k_y = 0$ m^{-1}, $k_z = 10.8$ m^{-1}, $K = 5$ kA/m, and $\varepsilon_{\mathrm{err}} = 1 \times 10^{-7}$. In this numerical analysis, a uniform mesh which includes 201 grid points (100 three-node elements) is used for the finite element discretization. The analytical and numerical results shown in this section are on the plane of $y = z = 0$ at $t = 2\pi l/\omega$, where l is an integer.

Fig. 4 shows the comparison between the analytical and numerical solutions. It is confirmed that the profile of $\mathrm{Im}(E_x)$ is in good agreement for the nonlinear case ($C_{\mathrm{sh}} = 0.6$). Since the large surface current yields high electric field strength, the instantaneous sheath voltage V_{sh} dominates the

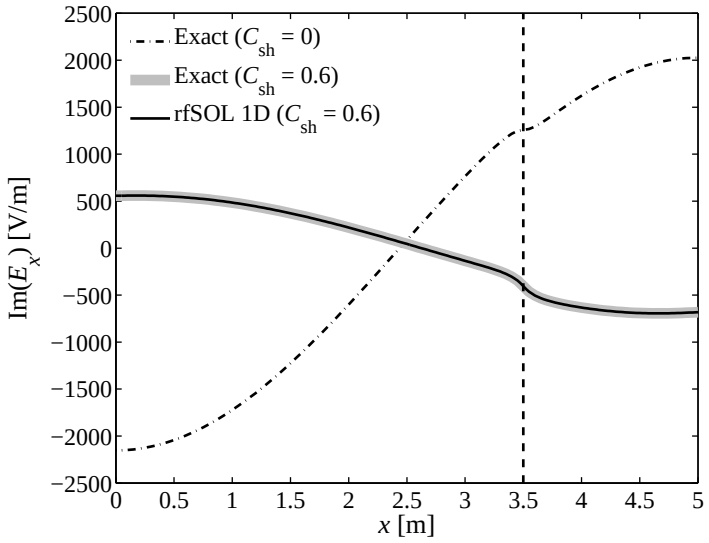

Figure 4: Comparison between the analytical and numerical solutions for the nonlinear sheath BC. The vertical dashed line indicates the antenna position. Note the verification of the rfSOL code with the analytic result, and the importance of the sheath BC (through C_{sh}) for this test.

Bohm sheath potential V_{B} in this problem; in fact, $C_{\mathrm{sh}}V_{\mathrm{sh}} = 8.8$ kV (the corresponding sheath width is $\Delta_{\mathrm{sh}} = 8.5$ mm), while $V_{\mathrm{B}} = 41$ V at the right boundary. The resultant enlarged sheath width can modify the whole profile of the electric field compared with the Bohm sheath model ($C_{\mathrm{sh}} = 0$) as shown in Fig. 4.

4.3. Insulating sheath limit

When we assume wave modes at the sheath-plasma interface, the sheath BC is expressed as

$$\boldsymbol{E}_{\mathrm{t}} = i\boldsymbol{k}_{\mathrm{t}}\frac{\Delta_{\mathrm{sh}}}{\varepsilon_{\mathrm{sh}}}D_{\mathrm{n}}, \tag{38}$$

where $\boldsymbol{k}_{\mathrm{t}}$ is the tangential wavenumber vector. The mathematical condition for sheaths to respond in the insulating sheath limit is $\left|\Delta_{\mathrm{sh}}k_{\parallel}\varepsilon_{\parallel}\sin\vartheta\right| > 1$. Here, let us consider the limit where $\Delta_{\mathrm{sh}} \to \infty$ for a finite current source. Since physically $\boldsymbol{E}_{\mathrm{t}}$ must be finite, it is required that $D_{\mathrm{n}} \to 0$. Consequently, the sheath becomes equivalent to an insulating layer, for which the boundary

condition (38) reduces to

$$D_{\rm n} = 0, \quad B_{\rm n} = 0. \tag{39}$$

The purpose of the numerical example presented below is to confirm that the developed numerical scheme possesses this property. However, we note that this is intended only for mathematical verification; in reality, an infinite sheath width clearly violates the thin-sheath limit ($|\boldsymbol{k}_{\rm t}|\,\Delta_{\rm sh} \ll 1$), which is a basis for deriving the sheath BC in the form of Eq. (4). (For realistic parameters, $|\boldsymbol{k}_{\rm t}|\,\Delta_{\rm sh} \ll 1$ is usually very well satisfied, even when the sheath BC approaches the insulating limit.)

For this demonstration, we consider a more general case where the plasma density is varied in the x direction and the background magnetic field is mostly in the toroidal (z) direction, but has a small x component. In this test problem, the calculation domain is defined such that $x_{\rm L} = 0$ m, $x_{\rm ant} = 0.155$ m, and $x_{\rm R} = 0.23$ m (see Fig. 3). The plasma density is assumed to vary according to the following formula:

$$n_0 = (n_{\rm L} - n_{\rm R}) \exp\left(-\frac{x - x_{\rm L}}{\lambda_n}\right) + n_{\rm R}, \tag{40}$$

where $n_{\rm L}$ and $n_{\rm R}$ are the density values at the left and right boundaries, respectively; these values are set at $n_{\rm L} = 2 \times 10^{19}$ m^{-3} and $n_{\rm R} = 2 \times 10^{16}$ m^{-3}. The length λ_n is chosen such that $x_{\rm R} - x_{\rm L} \gg \lambda_n$; here, $\lambda_n = 0.02$ m. The background magnetic field is set at $B_{0x} = 0.5$ T and $B_{0z} = 5.4$ T. The other fixed parameters are $f = 80$ MHz, $K = 1$ A/m, $k_y = 0$ m^{-1}, and $k_z = 10.8$ m^{-1}, and a piecewise uniform mesh of 3201 grid points (1600 three-node elements; 1080 elements in $x_{\rm L} \le x \le x_{\rm ant}$ and 520 elements in $x_{\rm ant} \le x \le x_{\rm R}$) is used.

To test the insulating sheath limit, the sheath width $\Delta_{\rm sh}$ is expressed as

$$\Delta_{\rm sh} = \alpha_{\rm amp} C_{\rm th} \lambda_{\rm De}, \tag{41}$$

where $\alpha_{\rm amp}$ is the artificial amplification factor. The discretized expressions corresponding to the insulating BC are, respectively, given by

$$\varepsilon^{\rm S}_{xx} \hat{E}^{\rm S}_{x{\rm i}} + \varepsilon^{\rm S}_{xy} \hat{E}^{\rm S}_{y{\rm i}} + \varepsilon^{\rm S}_{xz} \hat{E}^{\rm S}_{z{\rm i}} = 0, \tag{42}$$

$$k_y \hat{E}^{\rm S}_{z{\rm i}} - k_z \hat{E}^{\rm S}_{y{\rm i}} = 0, \tag{43}$$

where the subscript i denotes the nodes at the left and right boundaries.

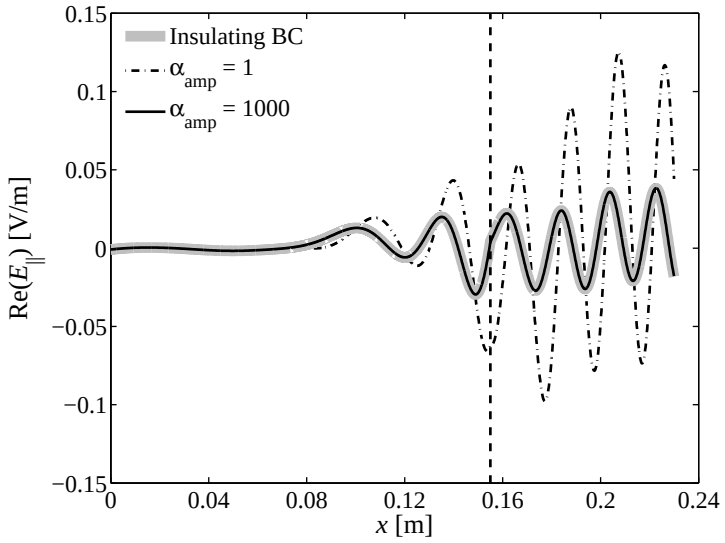

Figure 5: Demonstration that the sheath BC reduces to the insulating BC in the insulating sheath limit. The vertical dashed line indicates the antenna position.

Fig. 5 shows the comparison of the numerical results obtained by imposing the sheath BC with $\alpha_{\rm amp} = 1$, 1000 and the insulating BC. Of course, the condition for $\alpha_{\rm amp} = 1000$ is an extreme case, but is considered here as a numerical experiment. The calculations are conducted using the linear 1D rfSOL code for each case. (Here, the word "linear" comes from the fact that the sheath width is specified and thus nonlinearity does not enter in the system of discretized equations.) It is observed that the wave profile of $\mathrm{Re}\big(E_\parallel\big)$ for $\alpha_{\rm amp} = 1000$ is overlapped with the numerical result obtained using the insulating BC, which demonstrates that the present code yields the correct property in the insulating sheath limit.

In this problem the perpendicular and parallel wavenumber components can be expressed as

$$\begin{aligned} k_\perp &\simeq k_x, \\ k_\parallel &= b_x k_x + b_z k_z. \end{aligned} \tag{44}$$

Substituting Eq. (44) into the SW dispersion relation [28]

$$n_\perp^2 = \frac{\varepsilon_\parallel}{\varepsilon_\perp}\left(\varepsilon_\perp - n_\parallel^2\right) \tag{45}$$

($n_\parallel$ and $n_\perp$ are the parallel and perpendicular components, relative to the

background magnetic field $\boldsymbol{B}_0$, of the index of refraction defined as $\boldsymbol{n} = c\boldsymbol{k}/\omega$), we obtain a quadratic equation in terms of k_x:

$$C_{\mathrm{SW1}} k_x^2 + C_{\mathrm{SW2}} k_x + C_{\mathrm{SW3}} = 0, \tag{46}$$

where

$$\begin{aligned} &C_{\mathrm{SW1}} = \left(\frac{c}{\omega}\right)^2 \left(b_x^2 \varepsilon_\parallel + \varepsilon_\perp\right), \quad C_{\mathrm{SW2}} = 2\left(\frac{c}{\omega}\right)^2 b_x b_z \varepsilon_\parallel k_z, \\ &C_{\mathrm{SW3}} = \varepsilon_\parallel \left[\left(\frac{c}{\omega} b_z k_z\right)^2 - \varepsilon_\perp\right]. \end{aligned} \tag{47}$$

The roots of Eq. (46) are plotted in Fig. 6. It is confirmed that the numerically calculated wavelength around $x = 0.2$ m (shown in Fig. 5), which is approximately 0.02 m, agrees with the analytical estimate corresponding to the lower branch of $\mathrm{Re}(k_\perp)$. In addition, it is interesting to see that the lower hybrid resonance does not appear when the background magnetic field is slightly tilted to the walls. In fact, at the position where $\varepsilon_\perp = 0$, the electrostatic approximation ($n_\parallel^2 \gg \varepsilon_\perp$) is well satisfied, yielding a finite value of k_x:

$$k_x|_{\varepsilon_\perp = 0} = -\frac{b_z}{b_x} k_z. \tag{48}$$

For the given parameters this value of k_x is calculated at -117 m^{-1}.

4.4. Threshold-like turn-on variation in V_0

The last verification test of the 1D rfSOL code is directed to the problem including the propagating SW and sheath nonlinear interaction as shown in Fig. 7. Here, it is assumed that the sheath (or the metal wall) is present only on the right-hand side, while the SW is evanescent due to the absorbing layer on the left-hand side of the domain. Based on the notation in Fig. 7, the calculation domain is defined such that $x_{\mathrm{L}} = 0$ m, $x_{\mathrm{ant}} = 2.8$ m, and $x_{\mathrm{R}} = 3$ m; a sufficiently long distance is provided between the left boundary and the antenna position to assure that the left-going wave amplitude is smoothly decayed to zero within the absorbing layer and thereby it is not reflected from the left boundary. The plasma density and background magnetic field are assumed to be constant; $n_0 = 1 \times 10^{17}$ m^{-3}, and $B_{0x} = 1.5$ T, $B_{0y} = 0$ T, and $B_{0z} = 4$ T. The value of B_{0z} used here corresponds to a typical value of the toroidal background magnetic field in the edge region of the Alcator

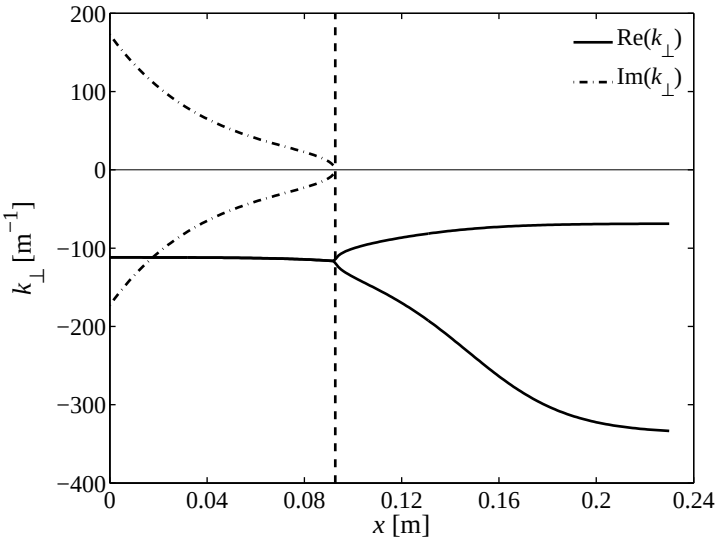

Figure 6: Plot of the real and imaginary parts of the perpendicular wavenumber component for the background magnetic field slightly inclined to the walls. The vertical dashed line indicates the position where $\varepsilon_\perp = 0$.

C-Mod tokamak for the hydrogen minority heating scenarios with the ICRF source frequency. The other parameters fixed in this analysis are $f = 80$ MHz, $T_\mathrm{e} = 10$ eV, $k_y = 0$ m^{-1}, $k_z = 10.8$ m^{-1}, $C_\mathrm{sh} = 0.6$, and $\varepsilon_\mathrm{err} = 1 \times 10^{-3}$; the absorbing layer is formed with $\nu_0 = 3 \times 10^{11}$ s^{-1}, $x_\mathrm{abs} = 0$ m, and $\lambda_\nu = 0.2$ m. In this numerical analysis a uniform mesh which includes 3001 grid points (1500 three-node elements) is used for the finite element discretization.

Fig. 8 shows the variations of the real part of the parallel electric field component ($E_\parallel = \boldsymbol{E} \cdot \boldsymbol{b}$) obtained with four different antenna current values. Here, the electric field is normalized by dividing it by the corresponding antenna current value; thus, changes in the profile of $\mathrm{Re}\big(E_\parallel\big)/K$ are entirely due to the dependence of the sheath width on the electric field strength. It is observed that the waves propagate with a constant wavelength until they are absorbed on the left-hand side.

An interesting observation is that the result for $K = 5000$ kA/m is almost overlapped with the result for $K = 500$ kA/m. This may be explained in a similar fashion to the insulating sheath limit described in Section 4.3. From the sheath BC, we obtain

$$\frac{|E_z|/K}{|D_\mathrm{n}|/K} = k_z \frac{\Delta_\mathrm{sh}}{\varepsilon_\mathrm{sh}}. \tag{49}$$

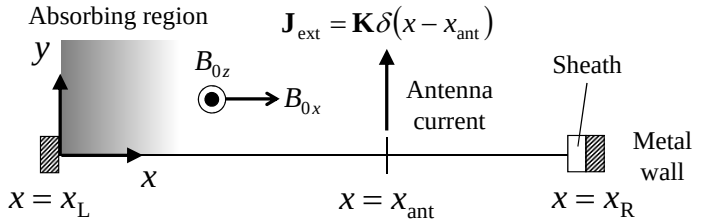

Figure 7: 1D calculation model for the propagating SW with the sheath BC imposed on the right wall.

Thus, when $|E_z|/K$ is unchanged with respect to K (or varied slowly compared with Δ_{sh}), $|D_{\text{n}}|/K$ should vary inversely with Δ_{sh}. In fact, this can be seen in Fig. 9; $|D_{\text{n}}|/K$ decreases with an increase of Δ_{sh} for sufficiently large values of K. Therefore, in the limit where $\Delta_{\text{sh}} \to \infty$, it is expected that the sheath BC will reduce to the quasi-insulating BC expressed as

$$D_{\text{n}}/K = 0, \quad B_{\text{n}} = 0. \tag{50}$$

The two cases for $K = 500$ and 5000 kA/m are essentially in this limit.

Fig. 10 shows the variation of the rectified sheath potential V_0 as a function of K, including the comparison with the Bohm sheath potential V_{B}. First, it is seen from Fig. 10a that the rectified sheath potential variation has a threshold-like turn-on characteristic, which is similar to the results obtained by the previous analytical work in Refs. [29, 30]. This characteristic is also observed in the variation of the sheath width shown in Fig. 9a due to the relation (8). For the present numerical condition, the sheath potential value and sheath width abruptly start increasing with the antenna current around $K = 20$ kA/m. It is important to realize that this threshold-like turn on is related to the nonlinearity of the sheath BC, and is distinct from the transition from the thermal sheath dominated regime (second term in Eq. (5)) to the RF sheath dominated regime (first term in Eq. (5)). As shown in Fig. 10b, this thermal-to-RF transition occurs around $K = 5$ kA/m, below which the entire system can be approximated as being linear since the Bohm sheath potential dominates the sheath potential.

5. RF sheath-plasma interactions in an Alcator C-Mod scale device

As a 2D numerical example, nonlinear RF sheath-plasma interaction problems are considered on a scale equivalent to the Alcator C-Mod de-

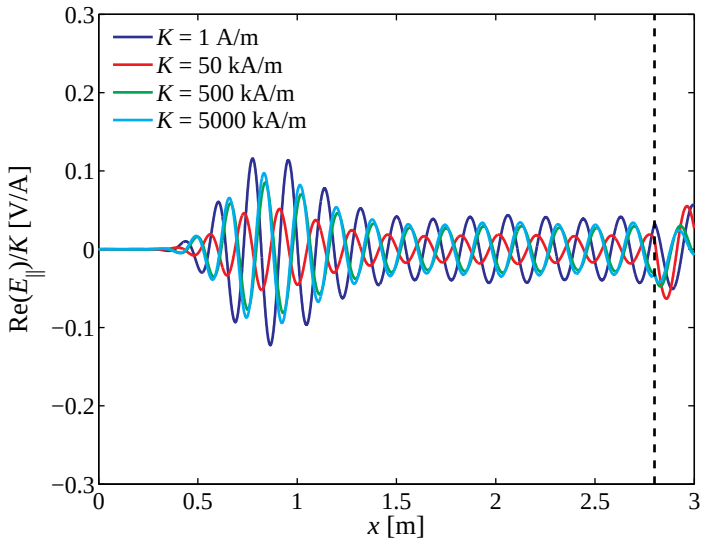

Figure 8: Plot of the real part of the normalized parallel electric field component along the 1D domain for four different surface current values. The vertical dashed line indicates the antenna position. These plots show propagating SWs.

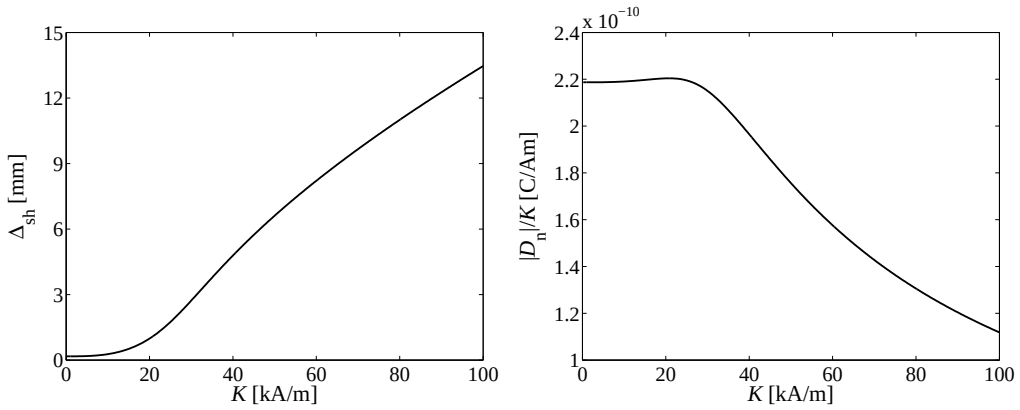

Figure 9: (a) The sheath width Δ_{sh} and (b) normalized normal component of the electric displacement $|D_{\mathrm{n}}|/K$ on the sheath surface as functions of the antenna current K.

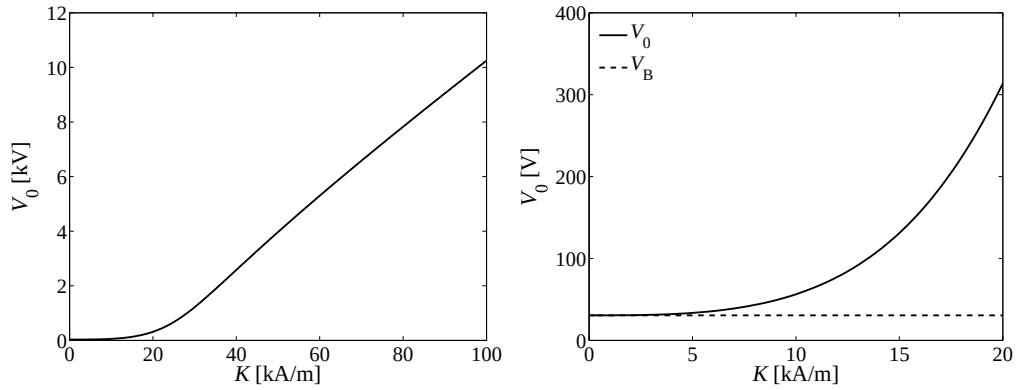

Figure 10: The rectified sheath potential V_0 as a function of the antenna current K: (a) entire variation; and (b) comparison with the Bohm sheath potential $V_{\rm B}$ in a restricted range of K.

vice. The left panel in Fig. 11 shows a schematic diagram of an Alcator C-Mod poloidal cross section with representative measurements. Here, this poloidal cross section is further simplified to a slab geometry by taking the long side of the slab as the circumferential length of the outer wall. With this approximation, the curvature effect of the wall is neglected. Other major approximations are (1) the plasma density is assumed to be constant; (2) relating to this, there are no reflected waves (due to the lower hybrid resonance) from the core plasma side; and (3) the background magnetic field is assumed to be spatially constant. The purpose of this section is to investigate the characteristic order of the sheath potential and its sensitivity to parameters in the RF sheath-plasma interactions in a large-size domain comparable to Alcator C-Mod.

The important scaling to assess the numerical results here is

$$V_0 \sim C_{\rm sh} V_{\rm sh} \sim \mathcal{C} \frac{\left(b_{\rm n} \varepsilon_\parallel E_\parallel\right)^4}{n_{\rm e0}^2 T_{\rm e}}, \tag{51}$$

where $\mathcal{C}$ is the product of fundamental constants, and $b_{\rm n}$ is the normal component (to the sheath) of the unit vector along the direction of the background magnetic field. Eq. (51) can be easily derived from Eqs. (5) in the RF-dominated limit (7), and the approximation that $D_{\rm n} \simeq \varepsilon_0 \varepsilon_\parallel E_\parallel b_{\rm n}$ for $\left|\varepsilon_\parallel\right| \gg |\varepsilon_\perp|, |\varepsilon_\times|$. Note that $E_\parallel$ at the sheath has a dependence on $b_{\rm n}$, $n_{\rm e0}$, and $T_{\rm e}$ through the sheath BC.

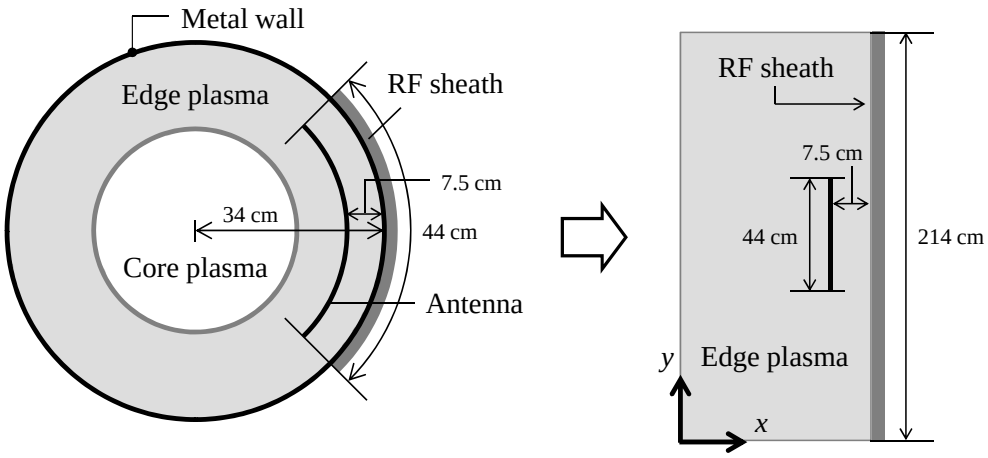

Figure 11: Schematic diagram of a simplified Alcator C-Mod poloidal cross section.

As shown in the right panel in Fig. 11, the calculation domain is a slab geometry, whose sides are aligned parallel to the x and y directions and measured at 3 m and $2.14\,(\simeq 2\pi \times 0.34)$ m, respectively. The antenna length $L_{\rm ant}$ and the distance between the antenna and the outer wall, $D_{\text{lw-ant}}$, are set at 0.44 m and 0.075 m, respectively. Here the electric field in the 2D slab geometry is numerically solved subject to the sheath BC on the right-hand side, the absorbing BC on the left-hand side, and a periodic BC at the top and bottom of the domain. The antenna surface current is given by a sine function in the y direction in such a way that the value at both ends is zero, which is achieved using the following expression:

$$\boldsymbol{J}_{\rm ext} = K\,(y)\,\delta\,(x - D_{\text{lw-ant}})\,\mathrm{e}^{i(k_z z - \omega t)}\boldsymbol{e}_y, \tag{52}$$

with

$$K\,(y) = \frac{K_{\max}}{2}\left\{\sin\left[\pi\left(\frac{2y - L_y + L_{\rm ant}}{L_{\rm ant}} - \frac{1}{2}\right)\right] + 1\right\}, \tag{53}$$

where $K_{\max}$ is the maximum antenna current density, L_y is the side length in the y direction, and it is assumed that the position $x = 0$ is located at the left boundary. The number of grid points is fixed at $921\,(x) \times 1201\,(y)$ (460×600 nine-node elements), and 81 grid points (40 grid elements) are provided between the antenna and the sheath (right wall). The absorbing layer on the left-hand side of the domain is formed with $\nu_0 = 2 \times 10^{11}$ s^{-1}

and $\lambda_\nu = 0.3$ m. The numerical results shown in this section are on the plane of $z = 0$ at $t = 2\pi l/\omega$.

The first numerical analysis is focused on the effect of the antenna current strength on the rectified sheath potential. Here, the plasma density and background magnetic field are assumed to be constant; $n_0 = 1 \times 10^{17}$ m^{-3}, and $B_{0x} = 1.5$ T, $B_{0y} = 0.5$ T, and $B_{0z} = 4$ T. The other parameters are fixed at $f = 80$ MHz, $T_\mathrm{e} = 10$ eV, $k_z = 10.8$ m^{-1}, $C_\mathrm{sh} = 0.6$, and $\varepsilon_\mathrm{err} = 1 \times 10^{-3}$.

Fig. 12 shows the filled contour plot of the real part of the parallel electric field component for $K_\mathrm{max} = 1$ A/m. Here, the antenna and magnetic field lines are also superimposed on the plot with black lines. It is observed that SWs are propagating along the field lines. As a 2D verification exercise, we have calculated the radial wavelength from the numerical solution in Fig. 12 and compared the result with that obtained from the electrostatic SW dispersion relation, $k_\perp^2 \varepsilon_\perp + k_\parallel^2 \varepsilon_\parallel = 0$, for the same parameters with $\lambda_y = 46$ cm (wavelength in the y direction, which is obtained from Fig. 12). Here, notice that both $k_\perp$ and $k_\parallel$ have dependence on k_x because of the field-line tilt. The SW dispersion relation yields roots at $k_x = -0.358$ and -0.311 cm^{-1}, which correspond to wavelengths of 17.5 cm and 20.2 cm. The measured wavelength of the modes in Fig. 12 is approximately 16.7 cm and in good agreement with the first mode. Further analysis reveals that the first mode has negative group velocity in the x direction (and hence is the mode we see to the left of the antenna), while the second mode has positive group velocity. A similar, but more accurate procedure is to use the full electromagnetic fourth order dispersion relation which, for these parameters, contains the propagating SW and the evanescent FW branches. Then, we find that the relevant SW root has $k_x = -0.370$ cm^{-1}, which corresponds to the wavelength of 17.0 cm. For $\lambda_y = 51$ cm, the electrostatic SW and full dispersion relations yield $\lambda_x = 17.8$ and 17.3 cm, respectively, which shows little sensitivity to relatively large uncertainty in λ_y. Thus, within uncertainties, the rfSOL code passes this 2D verification test.

Fig. 13 shows the profiles of the rectified sheath potential on the sheath surface, which are obtained with four different antenna current values. Compared to the result shown in Fig. 10, it is found that the potential value is significantly increased for the same strength of antenna current. Since the plasma density is the same in these cases, this increase is mostly attributed to the reduction in the antenna length (or increase in the gradient of the antenna current strength in its length direction; notice that the antenna length

for the 1D domain is regarded to be infinite).

Although the present model is geometrically too simplified for quantitative modeling of experiments, in this calculation we chose antenna parameters which are order-of-magnitude illustrative of Alcator C-Mod. Taking an antenna loading resistance of $R_{\rm ant} \sim 5$ Ohm, and using $I_{\rm ant}^2 R_{\rm ant} = P_{\rm RF}$ with an RF power level of $P_{\rm RF} \sim 1$ MW yields an antenna current of $I_{\rm ant} \sim 450$ A, or $K_{\rm max} \sim I_{\rm ant}/L_{\rm antw} \sim 4.5$ kA/m where $L_{\rm antw}$ (~ 0.1 m) is the antenna width. Thus, for moderate to high power operation, values of $K_{\rm max}$ in the range of kA/m are of interest, and they are even larger than what we have used here. On the other hand, according to Eq. (51), the sheath potential is proportional to $b_{\rm n}^4$. The value of $b_{\rm n}$ used here is probably larger than in the experiment. Finally, coupling to the SW is partly mitigated in realistic antennas by design, and the present 2D model problem does not include such effects, for example, the SW screening effect of an antenna box and Faraday shield. Thus, the model problem does not yield quantitative results for C-Mod, but establishes that significant sheath potentials may easily occur under worst case conditions.

In most cases, the sputtering effect starts to emerge when the sheath potential exceeds 100V [31]; thus, one can anticipate from these numerical results that the experimental configuration of Alcator C-Mod may lead to enhanced sputtering. Indeed, evidence for enhanced sputtering in the experiments has been reported in Refs. [10–12].

Next, a series of calculations is conducted to investigate the sheath potential variation depending on the plasma density and electron temperature with the antenna current and background magnetic field fixed. Fig. 14 shows the filled contour plot of the maximum rectified sheath potential $V_{\rm max}$ (on the sheath) as a function of the plasma density and electron temperature for $K_{\rm max} = 300$ A/m; the other parameters are unchanged from the previous calculations. It is seen that the sheath potential varies sensitively in the range of $n_0 = 1$–2×10^{17} m^{-3} and $T_{\rm e} = 5$–10 eV as predicted by the scaling (51), i.e., $V_0 \sim (n_{\rm e0}^2 T_{\rm e})^{-1}$. (Note that although $\varepsilon_\parallel$ depends on plasma density, $\varepsilon_\parallel E_\parallel$ remains approximately constant when plasma density is varied at fixed antenna current, because the parallel component of Eq. (1) implies that $J_{\rm ext\parallel} \sim \varepsilon_\parallel E_\parallel$.) Here, $n_{\rm LH}$ ($\propto B_0^2$) is the plasma density corresponding to the lower hybrid resonance ($\varepsilon_\perp = 0$; see Eq. (3)).

As a last numerical examination, spatial convergence has been verified for a sequence of uniform grids ranging from 10×20 to 320×640 nine-node elements. Here, the side length in the y direction, the antenna length, and

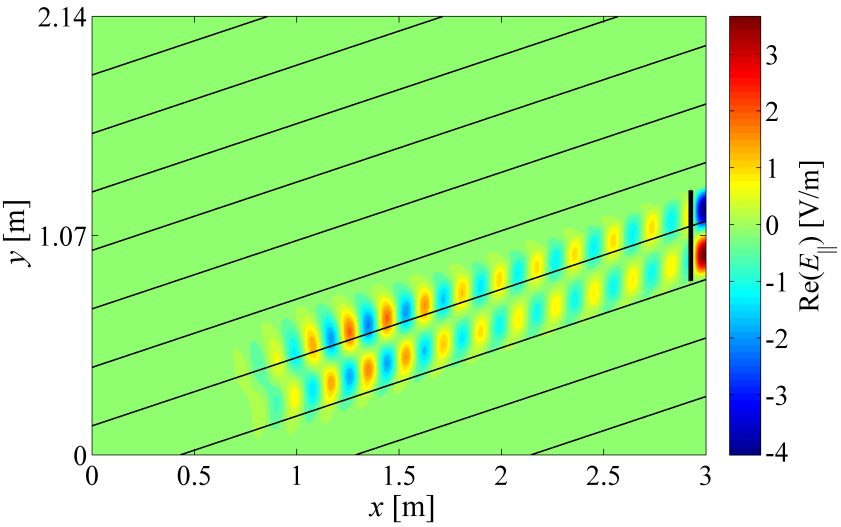

Figure 12: Filled contour plot of the real part of the parallel electric field component for $K_{\max} = 1$ A/m. This plot shows a propagating SW.

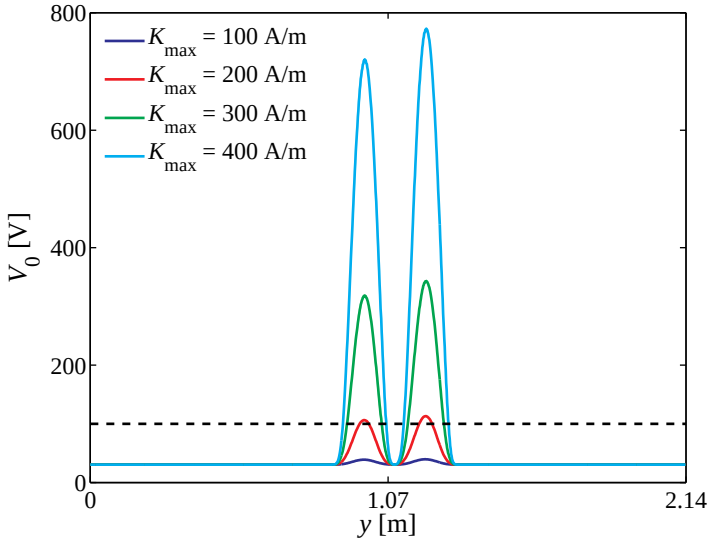

Figure 13: Rectified sheath potential vs. y for four different antenna current values. The horizontal dashed line indicates that $V_0 = 100$ V, which is where RF-induced sputtering would start to occur.

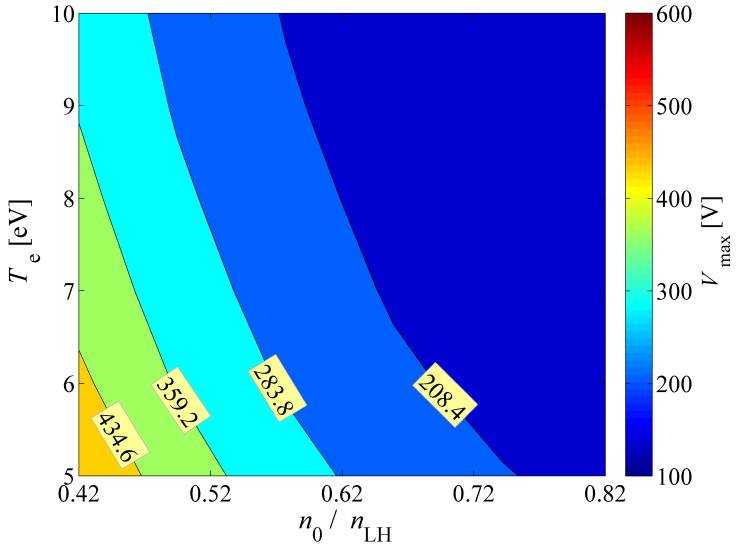

Figure 14: Filled contour plot of the maximum rectified sheath potential vs. plasma density and electron temperature for $K_{\max} = 300$ A/m.

the distance between the antenna and the sheath are slightly modified to 2 m, 0.5 m, and 0.6 m, respectively; other input parameters are the same as in the first numerical analysis of this section. We define a measure of relative spatial error by

$$\left\| \boldsymbol{E} - \boldsymbol{E}^{\mathrm{ref}} \right\|_{\mathrm{normalized}} = \left(\frac{\int_\Omega \left| \boldsymbol{E} - \boldsymbol{E}^{\mathrm{ref}} \right|^2 d\Omega}{\int_\Omega \left| \boldsymbol{E}^{\mathrm{ref}} \right|^2 d\Omega} \right)^{1/2}, \tag{54}$$

where $\boldsymbol{E}^{\mathrm{ref}}$ is the reference solution obtained by employing the finest resolution (320×640 grid elements). We find that the relative error is of order unity for 80×160 and coarser grids for $K_{\max} = 100$ A/m. The error decreases to 0.036 for the case of 160×320 grid elements indicating the onset of spatial convergence.

6. Conclusions

In this paper, we presented a numerical scheme that solves self-consistent RF sheath-plasma interactions in 1D and 2D domains for ICRF waves. The basic strategy is that a combined form of Maxwell's equations and the sheath

BC are both discretized by finite element methods, and the obtained discretized equations are combined into a vector equation. In addition, the numerical scheme is constructed with the aim of achieving a fast solver by applying (1) the central point approximation to the Jacobian and the components of the cofactor matrix in each integral of the discretized Maxwell's equation, and (2) the element-average technique to the sheath width in the discretization of the sheath BC. Owing to these techniques, the expression of the global matrix in the Newton-Raphson iteration is explicitly obtained without the necessity of using a numerical integration method. Furthermore, since the present scheme employs finite element methods, the scheme is appropriate for eventual application to complex boundary shapes that occur in realistic tokamak geometry.

The validity of the developed code was confirmed through comparisons with an analytical solution in the 1D closed domain and previous analytical results. Also, it was demonstrated in a 2D numerical example that the sheath potential value can reach on the order of hundred volts and sensitively varies depending on the plasma density and electron temperature. In a future paper, we will discuss some new properties of the RF sheath-plasma interactions, which are discovered using the present numerical code.

Acknowledgments

We would like to thank P.T. Bonoli and the RF SciDAC project for supporting this work, and J.C. Wright for his support in porting the rfSOL code to run on the computational facilities at NERSC. This work was supported by the U.S. DOE Contracts DE-FG02-91ER54109, DE-FC02-01ER54648, DE-FG02-97ER54392, and DE-FC02-05ER54823.

Appendix A. Element average and integrals in the sheath BC

The integrals which appear in the discretized sheath BC can be analytically calculated with reasonable approximations. The calculations are greatly simplified when the element average is applied to the derivative of $\Delta_{\rm sh}\kappa$ as shown in Eq. (26). The values of $\langle\Delta_{\rm sh}\rangle_{\rm e}$ and $\langle d\Delta_{\rm sh}/d\tau\rangle_{\rm e}$ are calculated as follows:

$$\langle\Delta_{\rm sh}\rangle_{\rm e} \equiv \frac{1}{\Gamma^{\rm S}_{\rm e}}\int_{\Gamma^{\rm S}_{\rm e}}\Delta_{\rm sh}d\Gamma^{\rm S} = \left(\frac{1}{\Gamma^{\rm S}_{\rm e}}\int_{\Gamma^{\rm S}_{\rm e}}N^{\rm S}_{\alpha}d\Gamma^{\rm S}\right)(\Delta_{\rm sh})_{\alpha} = A_{\alpha}\,(\Delta_{\rm sh})_{\alpha}\,, \quad \text{(A.1)}$$

$$\left\langle \frac{d\Delta_{\rm sh}}{d\tau} \right\rangle_{\rm e} \equiv \frac{1}{\Gamma_{\rm e}^{\rm S}} \int_{\Gamma_{\rm e}^{\rm S}} \frac{d\Delta_{\rm sh}}{d\tau} d\Gamma^{\rm S} = \left(\frac{1}{\Gamma_{\rm e}^{\rm S}} \int_{\Gamma_{\rm e}^{\rm S}} \frac{dN_\alpha^{\rm S}}{d\tau} d\Gamma^{\rm S} \right) (\Delta_{\rm sh})_\alpha = B_\alpha \, (\Delta_{\rm sh})_\alpha \, . \tag{A.2}$$

Here, $N_\alpha^{\rm S}$ is the local quadratic functions defined in a three-node element as follows:

$$N_\alpha^{\rm S} = \frac{\xi_\alpha \xi}{2} \left(1 + \xi_\alpha \xi\right) + \left(1 - \xi_\alpha^2\right) \left(1 - \xi^2\right), \tag{A.3}$$

where $-1 \leq \xi \leq 1$, and the subscript α denotes the local node number ($\alpha = 1, 2, 3$); $\xi_{1,2,3} = -1, 1, 0$. The coefficients A_α and B_α are given by

$$A_\alpha = \frac{1}{2} \left(\frac{4}{3} - \xi_\alpha^2 \right) \rightarrow A_1 = \frac{1}{6}, \quad A_2 = \frac{1}{6}, \quad A_3 = \frac{2}{3}, \tag{A.4}$$

$$B_\alpha = \frac{\xi_\alpha}{\Gamma_{\rm e}^{\rm S}} \rightarrow B_1 = -\frac{1}{\Gamma_{\rm e}^{\rm S}}, \quad B_2 = \frac{1}{\Gamma_{\rm e}^{\rm S}}, \quad B_3 = 0. \tag{A.5}$$

As a consequence of this approximation, we are only required to calculate the integrals shown in Eq. (28), whose calculations can be conducted over an element $\Gamma_{\rm e}^{\rm S}$ using the local shape functions $N_\alpha^{\rm S}$, $N_\beta^{\rm S}$, and $N_\gamma^{\rm S}$.

Appendix B. Newton-Raphson method

First of all, the present finite element equations are simply written as follows:

$$\boldsymbol{L} = \boldsymbol{R}, \tag{B.1}$$

with

$$\begin{aligned} \boldsymbol{L} = \big(& F_{x(1)}, \ldots, F_{x({\rm NP})}, \; F_{y(1)}, \ldots, F_{y({\rm NP})}, \; F_{z(1)}, \ldots, F_{z({\rm NP})}, \\ & F_{v(1)}, \ldots, F_{v({\rm NS+NA})}, \; G_{\tau(1)}, \ldots, G_{\tau({\rm NS})}, \; G_{z(1)}, \ldots, G_{z({\rm NS})}, \\ & H_{\tau(1)}, \ldots, H_{\tau({\rm NA})}, \; H_{z(1)}, \ldots, H_{z({\rm NA})} \big) \, , \end{aligned} \tag{B.2}$$

$$\boldsymbol{R} = \big(0, \ldots, 0, \; R_{y(1)}, \ldots, R_{y({\rm NP})}, \; 0, \ldots, 0 \big) \, , \tag{B.3}$$

where NP, NS, and NA are the numbers of nodes in the plasma, on the sheath surface, and on the core-edge plasma boundary, respectively, and the total number of nodes is expressed as NT (= NP + NS + NA); $H_{\tau i}$ and H_{zi}

correspond to the boundary condition on the core side, i.e., $\boldsymbol{E}_{\mathrm{t}} = \boldsymbol{0}$. Note that each number in the parenthesis in Eqs. (B.2) and (B.3) does not correspond to the global node number; instead it represents an independent equation. Also, the values of $R_{y(1)}, \ldots, R_{y(\mathrm{NP})}$ are mostly zero except the nodal values on the antenna current sheet. The task here is to find the solution $\hat{\boldsymbol{E}}^*$ of the equation

$$\boldsymbol{f}\left(\hat{\boldsymbol{E}}^*\right) = \boldsymbol{L} - \boldsymbol{R} = \boldsymbol{0} \tag{B.4}$$

through iterative calculations. In the present numerical analysis, $\boldsymbol{f}$ is treated as being a real vector by splitting the components of $\boldsymbol{L}$ and $\boldsymbol{R}$ into real and imaginary parts.

Let us assume that an intermediate solution $\hat{\boldsymbol{E}}^{(n)}$ is evaluated in the n-th iteration. Then, a set of linear equations for the correction $\delta\hat{\boldsymbol{E}}$ is obtained by applying a Taylor series expansion to Eq. (B.4) and then neglecting high-order terms of the resultant equation as follows:

$$\boldsymbol{K}^{(n)} \cdot \delta\hat{\boldsymbol{E}} = -\boldsymbol{f}\left(\hat{\boldsymbol{E}}^{(n)}\right), \tag{B.5}$$

where

$$\boldsymbol{K}^{(n)} = \left(\nabla_{\hat{\boldsymbol{E}}}\boldsymbol{f}\right)^{\mathrm{T}}\Big|_{\hat{\boldsymbol{E}}^{(n)}}. \tag{B.6}$$

Here, $\nabla_{\hat{\boldsymbol{E}}}$ is the nabla operator with respect to $\hat{\boldsymbol{E}}$ in the abstract space of dimension NT, and T is the transpose operation. Notice that the expression of $\boldsymbol{K}^{(n)}$ is explicitly obtained using the discretized equations (18), (27), and (31). A procedure to obtain the derivative expressions of the discretized sheath BC is partly demonstrated in Appendix C for a flat wall.

The intermediate solution is then improved by adding the correction:

$$\hat{\boldsymbol{E}}^{(n+1)} = \hat{\boldsymbol{E}}^{(n)} + \delta\hat{\boldsymbol{E}}. \tag{B.7}$$

The process is iteratively conducted until the solution is fully converged. The present scheme adopts the following convergence criterion:

$$\left.\frac{\left|\delta\hat{E}_{xj}\right|}{\left|\hat{E}_{xj}^{(n+1)}\right|}, \quad \frac{\left|\delta\hat{E}_{yj}\right|}{\left|\hat{E}_{yj}^{(n+1)}\right|}, \quad \frac{\left|\delta\hat{E}_{zj}\right|}{\left|\hat{E}_{zj}^{(n+1)}\right|}\right|_{\max} < \varepsilon_{\mathrm{err}}, \tag{B.8}$$

where the subscript j denotes the global node number, and $\varepsilon_{\rm err}$ is a parameter which may be adjusted depending on the problems; in general, the condition where $\varepsilon_{\rm err} \sim 10^{-3}$ yields an accurate solution. In the present numerical analyses, we also check the convergence of the norm of the residual vector in order to confirm that the error sufficiently reduces from a global point of view.

Appendix C. Derivative expressions of the discretized sheath BC

The global matrix $\boldsymbol{K}^{(n)}$ appeared in the Newton-Raphson iteration algorithm can be explicitly obtained using the discretized governing equations derived in Section 3. In this appendix, a procedure to obtain the derivative expressions of the discretized sheath BC is partly demonstrated. Although the calculations are straightforward, they will clarify the effectiveness of the element-average technique since this method greatly simplifies the derivation of the derivative expressions.

For simplicity, let us consider the case where the sheath BC is imposed on a flat wall lying in the y-z plane. In that case, the corresponding discretized sheath BC on the left wall is given by

$$G_{yi} = \sum_m G_{yi}|_{{\rm e}(m)} = \sum_m \left(\left[N_i^{\rm S} N_j^{\rm S} \right] \hat{E}_{yj}^{\rm S} - \mathcal{S}_{ijk}^{y{\rm L}} \kappa_{jk} \right) \Big|_{{\rm e}(m)} = 0, \tag{C.1}$$

$$G_{zi} = \sum_m G_{zi}|_{{\rm e}(m)} = \sum_m \left(\left[N_i^{\rm S} N_j^{\rm S} \right] \hat{E}_{zj}^{\rm S} - i\mathcal{S}_{ijk}^{z{\rm L}} \kappa_{jk} \right) \Big|_{{\rm e}(m)} = 0, \tag{C.2}$$

where

$$\begin{aligned}
&\mathcal{S}_{ijk}^{y{\rm L}} = \mathcal{T}_{ijkl}^{y{\rm L}} \left(\Delta_{\rm sh} \right)_l , \quad \mathcal{S}_{ijk}^{z{\rm L}} = \mathcal{T}_{ijkl}^{z{\rm L}} \left(\Delta_{\rm sh} \right)_l , \\
&\mathcal{T}_{ijkl}^{y{\rm L}} = A_l^{{\rm e}(m)} \left[N_i^{\rm S} \check{N}_j^{\rm S} \check{N}_k^{\rm S} \right] + B_l^{{\rm e}(m)} \left[N_i^{\rm S} N_j^{\rm S} N_k^{\rm S} \right] , \\
&\mathcal{T}_{ijkl}^{z{\rm L}} = k_z A_l^{{\rm e}(m)} \left[N_i^{\rm S} N_j^{\rm S} N_k^{\rm S} \right] , \\
&\kappa_{jk} = \varepsilon_{xxk}^{\rm S} \hat{E}_{xj}^{\rm S} + \varepsilon_{xyk}^{\rm S} \hat{E}_{yj}^{\rm S} + \varepsilon_{xzk}^{\rm S} \hat{E}_{zj}^{\rm S} .
\end{aligned} \tag{C.3}$$

Here, note that the element-averaged sheath width and its derivative are expressed as

$$\begin{aligned}
&\left\langle \Delta_{\rm sh} \right\rangle_{{\rm e}(m)} = A_l^{{\rm e}(m)} \left(\Delta_{\rm sh} \right)_l , \\
&\left\langle \frac{d\Delta_{\rm sh}}{dy} \right\rangle_{{\rm e}(m)} = B_l^{{\rm e}(m)} \left(\Delta_{\rm sh} \right)_l ,
\end{aligned} \tag{C.4}$$

where the subscript l denotes the global node number. The coefficients $A_l^{\mathrm{e}(m)}$ and $B_l^{\mathrm{e}(m)}$ are defined such that they possess specific values given by Eqs. (A.4) and (A.5) at the grid nodes constituting the element $\mathrm{e}(m)$ and their values are zero at the other nodes. The expression of $G_{yi}|_{\mathrm{e}(m)}$ in Eq. (C.1) is easily divided into real and imaginary parts as follows:

$$\begin{aligned} G_{yi}^{(\mathrm{R})}\Big|_{\mathrm{e}(m)} &= \left[N_i^{\mathrm{S}} N_j^{\mathrm{S}}\right] \hat{E}_{yj}^{\mathrm{S(R)}} - \mathcal{S}_{ijk}^{y\mathrm{L}} \kappa_{jk}^{(\mathrm{R})}, \\ G_{yi}^{(\mathrm{I})}\Big|_{\mathrm{e}(m)} &= \left[N_i^{\mathrm{S}} N_j^{\mathrm{S}}\right] \hat{E}_{yj}^{\mathrm{S(I)}} - \mathcal{S}_{ijk}^{y\mathrm{L}} \kappa_{jk}^{(\mathrm{I})}, \end{aligned} \tag{C.5}$$

where the superscripts R and I denote the real and imaginary parts of the quantity, respectively. Notice that $\mathcal{S}_{ijk}^{y\mathrm{L}}$ and $\mathcal{S}_{ijk}^{z\mathrm{L}}$ are real values. Recalling that the sheath width is expressed as

$$(\Delta_{\mathrm{sh}})_l = \left(\alpha_{\mathrm{sh}} |\kappa|^3 + \beta_{\mathrm{sh}}\right)_l, \tag{C.6}$$

where

$$\alpha_{\mathrm{sh}} = \left(\frac{eC_{\mathrm{sh}}}{T_{\mathrm{e}}}\right)^3 \lambda_{\mathrm{De}}^4, \quad \beta_{\mathrm{sh}} = C_{\mathrm{th}} \lambda_{\mathrm{De}}, \tag{C.7}$$

for example, the derivative expression of $G_{yi}^{(\mathrm{R})}\Big|_{\mathrm{e}(m)}$ with respect to $\hat{E}_{xn}^{\mathrm{S(R)}}$ (where the subscript n denotes the global node number) is given by

$$\begin{aligned} \frac{\partial G_{yi}^{(\mathrm{R})}}{\partial \hat{E}_{xn}^{\mathrm{S(R)}}}\Bigg|_{\mathrm{e}(m)} &= -\frac{\partial \mathcal{S}_{ijk}^{y\mathrm{L}}}{\partial \hat{E}_{xn}^{\mathrm{S(R)}}} \kappa_{jk}^{(\mathrm{R})} - \mathcal{S}_{ijk}^{y\mathrm{L}} \frac{\partial \kappa_{jk}^{(\mathrm{R})}}{\partial \hat{E}_{xn}^{\mathrm{S(R)}}} \\ &= -\mathcal{T}_{ijkn}^{y\mathrm{L}} \left(\alpha_{\mathrm{sh}}\right)_n \frac{\partial |\kappa_n|^3}{\partial \hat{E}_{xn}^{\mathrm{S(R)}}} \kappa_{jk}^{(\mathrm{R})} - \mathcal{S}_{ink}^{y\mathrm{L}} \varepsilon_{xxk}^{\mathrm{S(R)}} \\ &= -3\mathcal{T}_{ijkn}^{y\mathrm{L}} \kappa_{jk}^{(\mathrm{R})} \left(\alpha_{\mathrm{sh}}\right)_n |\kappa_n| \left(\kappa_n^{(\mathrm{R})} \varepsilon_{xxn}^{\mathrm{S(R)}} + \kappa_n^{(\mathrm{I})} \varepsilon_{xxn}^{\mathrm{S(I)}}\right) - \mathcal{S}_{ink}^{y\mathrm{L}} \varepsilon_{xxk}^{\mathrm{S(R)}}. \end{aligned}$$

Here, it is assumed that the node n is included in the element $\mathrm{e}(m)$. Note that the summation convention does not apply to the subscript n, and $\varepsilon_{xxk}^{\mathrm{S}}$ has both real and imaginary parts due to the assumption that the electron mass is a complex-valued quantity (see Section 2). Following the same procedure, one can obtain the derivative expressions of $G_{yi}^{(\mathrm{R})}\Big|_{\mathrm{e}(m)}$ with respect to the other real and imaginary parts of the electric field components (and the derivatives of $G_{yi}^{(\mathrm{I})}\Big|_{\mathrm{e}(m)}$; see Ref. [26] for the results).

References

[1] J.P. Freidberg, Plasma Physics and Fusion Energy, Cambridge University Press, 2007.

[2] J. Wesson, Tokamaks (third edition), Oxford University Press, 2004.

[3] F.W. Perkins, *IEEE Trans. Plasma Sci.* 12 (1984) 53–63.

[4] F.W. Perkins, *Nucl. Fusion* 29 (1989) 583–592.

[5] J.-M. Noterdaeme, G. Van Oost, *Plasma Phys. Control. Fusion* 35 (1993) 1481–1511.

[6] J.R. Myra, et al., *Nucl. Fusion* 46 (2006) S455–S468.

[7] J.R. Myra, D.A. D'Ippolito, M.J. Gerver, *Nucl. Fusion* 30 (1990) 845–858.

[8] D.A. D'Ippolito, J.R. Myra, M. Bureš, J. Jacquinot, *Plasma Phys. Control. Fusion* 33 (1991) 607–642.

[9] M. Bureš, et al., *Plasma Phys. Control. Fusion* 33 (1991) 937–967.

[10] B. Lipschultz, et al., *Nucl. Fusion* 41 (2001) 585–596.

[11] S.J. Wukitch, et al., *Proc. 21st IAEA Fusion Energy Conf.* (Chengdu, China, 16–21 October 2006) IAEA-CN-149/FT/1–6.

[12] S.J. Wukitch, et al., *Proc. 22nd IAEA Fusion Energy Conf.* (Geneva, Switzerland, 13–18 October 2008) EX/P6–23.

[13] L. Colas, et al., *Nucl. Fusion* 46 (2006) S500–S513.

[14] J. Hosea, et al., *Phys. Plasmas* 15 (2008) 056104.

[15] E.F. Jaeger, L.A. Berry, J.S. Tolliver, D.B. Batchelor, *Phys. Plasmas* 2 (1995) 2597–2604.

[16] M.D. Carter, et al., *J. Appl. Phys.* 100 (2006) 073305.

[17] M.A. Lieberman, *IEEE Trans. Plasma Sci.* 16 (1988) 638–644.

[18] V.A. Godyak, N. Sternberg, *Phys. Rev. A* 42 (1990) 2299–2312.

[19] J.R. Myra, D.A. D'Ippolito, M. Bures, *Phys. Plasmas* 1 (1994) 2890–2900.

[20] D.A. D'Ippolito, J.R. Myra, *Phys. Plasmas* 13 (2006) 102508.

[21] D.N. Smithe, *Journal of Physics*: Conference Series 78 (2007) 012069.

[22] B. Van Compernolle, et al., *Proc. 35th EPS Conf. on Plasma Physics* (Hersonissos, Crete, Greece, 9–13 June 2008) 32F (ECA) P–2.105.

[23] C.D. Child, *Phys. Rev. (Series I)* 32 (1911) 492–511.

[24] I. Langmuir, *Phys. Rev.* 21 (1923) 419–435.

[25] K.J. Bathe, Finite Element Procedures, Prentice-Hall, 1996.

[26] H. Kohno, Numerical analysis of radio-frequency sheath-plasma interactions in the ion cyclotron range of frequencies, Sc.D. thesis, MIT, 2011.

[27] W.H. Press, S.A. Teukolsky, W.T. Vetterling, B.P. Flannery, Numerical Recipes: The Art of Scientific Computing (third edition), Cambridge University Press, 2007.

[28] T.H. Stix, Waves in Plasmas, American Institute of Physics, 1992.

[29] J.R. Myra, D.A. D'Ippolito, *Phys. Rev. Lett.* 101 (2008) 195004.

[30] D.A. D'Ippolito, J.R. Myra, *Phys. Plasmas* 16 (2009) 022506.

[31] R.A. Langley, et al., Data Compendium for Plasma-Surface Interactions, (*Nucl. Fusion*, Special Issue, IAEA, Vienna 1984); *Nucl. Fusion* 24 (1984) 1683 (Corrigenda).